WILEY-VCH

# Soft Robotic-Adapted Multimodal Sensors Derived from Entirely Intrinsic Self-Healing and Stretchable Cross-Linked Networks

*Xingyi Dai[1], Yinghui Wu[1], Qihua Liang[1], Jingkun Yang[1], Long-Biao Huang[1]\*, Jie Kong[2]\*, Jianhua Hao[3]\**

[1]Dr. X. Dai, Dr. Y. Wu, Q. Liang, J. Yang, Dr. L.-B. Huang
College of Physics and Optoelectronic Engineering
Shenzhen University, Shenzhen, 518060, P. R. China
*Corresponding Author, E-mail: huanglb@szu.edu.cn

[2]Prof. J. Kong
MOE Key Laboratory of Materials Physics and Chemistry in Extraordinary Conditions,
Shaanxi Key Laboratory of Macromolecular Science and Technology, School of Chemistry and Chemical Engineering,
Northwestern Polytechnical University, Xi'an, 710072, P. R. China.
*Corresponding Author, E-mail: kongjie@nwpu.edu.cn

[3]Prof. J. Hao
Department of Applied Physics
The Hong Kong Polytechnic University, Hong Kong, P. R. China
*Corresponding Author, E-mail: jh.hao@polyu.edu.hk

**Abstract**

Flexible sensing technologies that play a pivotal role in endowing robots with detection capabilities and monitoring their motions are impulsively desired for intelligent robotics systems. However, integrating and constructing reliable and sustainable flexible sensors with multifunctionality for robots remains an everlasting challenge. Here, we develop an entirely intrinsic self-healing, stretchable, and attachable multimodal sensor that can be conformally integrated with soft robots to identify diverse signals. The dynamic bonds cross-linked networks including the insulating polymer and conductive hydrogel with good comprehensive performances are designed to fabricate the sensor with prolonged lifespan and improved reliability. Benefiting from the self-adhesiveness of the hydrogel, strong interfacial bonding can be formed on various surfaces, which promotes the conformable integration of the sensor with robots. Due to the ionic transportation mechanism, the sensor could detect strain and temperature based on piezoresistive and thermoresistive effect, respectively. Moreover, the sensor can work in triboelectric mode to achieve self-powered sensing. Various information could be identified from the electrical signals generated by the sensor, including hand gestures, soft robot crawling motions, a message of code, the temperature of objects, and the type of materials, holding great promise in the fields of environmental detection, wearable devices, human-machine interfacing, and robotics.

# 1. Introduction

With the advancement of "Industry 4.0", considerable and praiseworthy advances in robotics have been made, which can assist or replace humans to complete specific tasks, especially complicated and dangerous ones under harsh conditions.[1,2] Robotics have permeated the broad areas of the manufacturing, construction, and medical industry.[3] In the meantime, sensing technology has been proven significant in data collection on robots to enable them to perform the relevant operations effectively and accurately.[4-6] The sensors can empower robots with human-like capabilities and monitor their motions.[7,8] Compared with traditional rigid sensors, flexible sensors have the extraordinary advantages of high conformability and dexterity to conveniently complete detection for either rigid or soft robots.[9] The sensing mechanism is mainly based on piezoresistive, capacitive, piezoelectric, and triboelectric effects.[10-14] A variety of signals can be detected, such as pressure, deformation, temperature, humidity, gas, and targeted materials.[15-20] While, most sensors have the restriction of single function and complex preparation methods, and it is difficult to realize the perception of diverse signals by a single sensor. Therefore, the facile multifunction integration of sensors suitable for robotics is imperative, and the relevant study remains challenging.

In addition to sensing functions, the intrinsic performances of the sensors derived from functional materials, such as adhesion, conformability, self-healing ability, stretchability, and environmental resistance, count a great deal in practical applications.[21-23] For flexible sensors, the attachable capability is one of the critical elements in achieving accurate detection.[24] It is highly expected to tightly integrate the sensor with the target such as the human body, rigid objects, or soft robots.[25] Self-adhesive hydrogel with low modulus and deformability is an ideal candidate to realize the conformable match and robust interfacial bonding on dynamically curved surfaces.[26-28] Meanwhile, the conductivity of hydrogel based on ionic or electron transportation can promote the sensing function.[29,30] While the dehydration and freeze of hydrogels are nonnegligible issues. Some approaches could be adopted, such as the

incorporation of salts, cryoprotectants, and strong molecular interactions.[31-33] In addition, insulating polymers also play a vital role in flexible sensors, owing to their diverse functions as encapsulation layers to ensure safety and effectiveness, and as electrification layers to realize the triboelectric effect and self-powered sensing.[34-36] Therefore, the flexible sensors constructed by conductive hydrogel and insulating polymers are exceptionally attractive. However, since flexible sensors may be exposed to long-time service and complex force status, the materials could be damaged to failure. For overcoming the barrier, those materials with intrinsic self-healing ability and stretchability are of great significance to enhance reliability and durability.[37-40] Thus, the reliable flexible sensors capable of possessing multiple perception functions remain to be explored.

Herein, a soft robotic-adapted multimodal sensor with self-healing, stretchable, and attachable features was presented, which could be conformally integrated with robots to sense strain, temperature, motions, and materials. An imine and hydrogen bond-based dual cross-linked polymer and a hydrogen bond-based hydrogel were designed and synthesized, both of which were provided with flexible, stretchable, and self-healing properties. Besides, the hydrogel had the characteristic of conductivity, self-adhesiveness, and temperature tolerance. The polymer and hydrogel served as dielectric and electrode layers, respectively, to construct the multimodal sensor which could meet the challenge of mechanical damage, deformation, and extreme environments. Thanks to the self-adhesiveness, the robust integration of the sensor on diverse surfaces could be achieved. Meanwhile, combined with flexibility and stretchability, conformal interfaces could be formed between the sensor and robots, enabling the sensor's effective operation. The sensor could work in piezoresistive, thermoresistive, or triboelectric mode, thus detecting different changes, such as strain, temperature, and materials. Through analyzing the electrical signals collected from the sensor, various information could be acquired, including hand gestures, messages of Morse code, temperature of objects, soft robot crawling motions, and type of materials. This work may provide a meaningful strategy for the

development of reliable and sustainable multifunctional sensors for wearable devices, human-machine interfacing, and robotics.

## 2. Results and Discussion

### 2.1. Design and preparation of materials

To enable a soft robotic-adapted multimodal sensor with entirely intrinsic self-healing, stretchable, attachable, and conformable properties, the functional polymer materials for dielectric and electrode layers were designed and prepared, respectively. The schematic illustration of the synthesis process of imine and hydrogen bonds-based polyurea (IH-PUa) is depicted in **Figure 1**a. The isophorone diisocyanate (IPDI) reacted with excessive poly(propylene glycol)bis(2-aminopropyl ether) (PEA) to obtain the amino terminated linear PUa prepolymer (Figure S1, Supporting Information), in which the PEA macromolecule chain served as the soft segment and the urea groups could form hydrogen bonding interactions. Then, terephthalaldehyde (TPA) reacted with tris(2-aminoethyl)amine (TAEA) and linear PUa prepolymer through the Schiff-base reaction between amino and aldehyde groups to generate imine bonds. Based on the dual cross-linking of imine and hydrogen bonds, the polymerization of the IH-PUa polymer was completed. Comparing the FTIR spectra of the monomers and polymer, it can be observed that the peak of the isocyanate bonds at 2272 cm$^{-1}$ and the peak of the aldehyde group at 1685 cm$^{-1}$ have almost disappeared in the spectra of IH-PUa. Meanwhile, there is a new peak at 1643 cm$^{-1}$ ascribed to the -CH=N- bond, confirming the formation of the IH-PUa polymer (Figure S2, Supporting Information).

**Figure 2**a presents the chemical structure of the hydrogen bond-based polyacrylamide-clay-trehalose (PAAm-Clay-T) hydrogel which was polymerized between acrylamide (AAm), synthetic hectorite clay, and trehalose. Based on the in-situ free radical reaction, AAm monomer was initiated to polymerize with the formation of PAAm which interacted with nanoclay and trehalose via hydrogen bonds. As shown in Figure S3 (Supporting Information), the peak at

1660 cm$^{-1}$ is ascribed to the stretching vibration of the -C=O group of amide, and the stretching vibration of -CH$_2$- of PAAm chain can be observed at 2965 cm$^{-1}$, indicating the successful polymerization. In addition, the trehalose was introduced to the network to form strong hydrogen bond interactions, to improve the mechanical property and temperature tolerance of the hydrogel.[33] Eventually, the IH-PUa polymer and PAAm-Clay-T hydrogel could be assembled as a multimodal sensor for robotics.

## 2.2. Performance of IH-PUa polymer

The self-healing and mechanical performances of IH-PUa polymer were systematically investigated. As shown in Figure 1b, the optical microscopic images reveal the change in the damaged area of the IH-PUa when being cut and after healing. The crack of about 20 μm almost disappeared, intuitively reflecting the self-healing ability of this material. Next, the uniaxial tensile tests were carried out for the quantitative characterization of mechanical behaviors. Figure 1c shows the stress-strain curves of the specimens with different healing times (6 h, 12 h, and 24 h) at 25 °C. The original IH-PUa specimen exhibited high stretchability with the elongation at a break of 1045%, and the maximum stress was 1.79 MPa. For the broken specimen with a healing time of 6 h, the mechanical performance was relatively weaker with the elongation at a break of 500% and maximum stress of 0.76 MPa. With the increment of healing time, the mechanical performances of the healed sample were gradually enhanced. When the healing time was maintained for 24 h, the mechanical performance almost recovered with the elongation at a break of 1028% and the maximum stress of 1.75 MPa. The self-healing efficiency is defined as the ratio of fracture strain of the healed sample to that of the original sample.[41] The IH-PUa showed excellent self-healing efficiency of 98.4%.

The intrinsic self-healing mechanism of IH-PUa could be attributed to the synergistic effects of dynamic imine and hydrogen bonds (Figure 1a). On the one hand, the imine bonds were cleaved into amino and aldehyde groups in the damaged area. During the healing process,

the imine bonds could be reformed at the fractured interfaces. Meanwhile, the exchange and metathesis of imine bonds could occur.[42] On the other hand, the hydrogen bonds between urea groups could be dissociated and associated,[43] synergistically promoting IH-PUa self-healing. Moreover, the glass transition temperature ($T_g$) of IH-PUa was about −50 $^o$C (Figure S4, Supporting Information), which was low enough to enable the mobility of the chain segments to assist the coupling of reversible groups and the fusion of the interface. In addition, the temperature had a significant influence on the self-healing process of IH-PUa. Figure 1d depicts the stress-strain curves of the specimens healing at different temperatures (25 $^o$C, 50 $^o$C, and 80 $^o$C). With the healing temperature rising, the healing effect was significantly improved. The fracture strain and maximum stress of the specimen could separately reach 982% and 1.76 MPa at 80 $^o$C for 3 h, with a healing efficiency of 94%. At high temperatures, the molecular activity increased, leading to the faster reversible reactions of dynamic bonds.

## 2.3. Performance of PAAm-Clay-T hydrogel

The self-healing, mechanical, and electrical performances of PAAm-Clay-T hydrogel were systemically investigated. From the photographs of the stretching process, the ultra-high stretchability of the PAAm-Clay-T hydrogel can be observed (Figure 2b). Additionally, the mechanically self-healing properties of PAAm-Clay-T hydrogel were quantitatively characterized, as shown in Figure 2c. The PAAm-Clay-T hydrogel exhibited high elongation at a break of 4052% and maximum stress of 0.11 MPa. After healing for 2 h at 25 $^o$C, the healed hydrogel could be stretched to 4009% with the self-healing efficiency up to 98.9%, and the maximum stress could recover to 0.1 MPa. Figure 2d shows the optical microscopic images of the PAAm-Clay-T hydrogel after cutting and healing. There was a crack when the hydrogel was cut from the middle into half using a blade and then to be in contact. While the crack almost disappeared after a healing process. Owing to the hydrogen bond interaction between the amido group and nanoclay, the PAAm-Clay-T hydrogel was endowed with intrinsic self-healing

properties. Under the mechanical force, the hydrogen bonds were dissociated. During the healing process, the hydrogen bonds could be associated again at the fractured interface, due to the reversibility of hydrogen bonds. Moreover, the PAAm-Clay-T hydrogel remains unpierced even when sharp nails are driven into it, showing good puncture-resistance (Figure 2e).

Besides good mechanical and self-healing properties, the PAAm-Clay-T hydrogel showed good conductivity. The sodium cations ($Na^+$) from the nanoclay permeated in the hydrogel networks, leading to the ionic conductivity of the PAAm-Clay-T. As shown in Figure 2f, the impedance magnitude ($|Z|$) and negative phase angle ($-\phi$) decrease with frequency varying from 100 Hz to 100 kHz, indicating the impedance frequency dependency of the PAAm-Clay-T hydrogel. Figure 2g shows the typical Nyquist plot of the impedance spectrum of the hydrogel at room temperature, and the intrinsic bulk resistance ($R_b$) is as low as 10 $\Omega$, the value of which can be obtained from the point where the fitting plot intersects the $Z'$-axis. Furtherly, the conductivity ($\sigma$) could be calculated by the equation $\sigma = L/R_b S$, in which $L$ and $S$ represent the thickness and area of the sample, respectively.[44] The conductivity of PAAm-Clay-T hydrogel was $9.95 \times 10^{-2}$ S cm$^{-1}$ at 25 °C, indicating high ionic conductive capability. Moreover, the PAAm-Clay-T hydrogel exhibited good conductive properties at a broad temperature range. As shown in Figure 2h, when the temperature increases from $-10$ °C to 60 °C, the conductivity of the PAAm-Clay-T hydrogel shows an upward trend. The conductivity is about $0.51 \times 10^{-2}$ S cm$^{-1}$ at $-10$ °C and $12.4 \times 10^{-2}$ S cm$^{-1}$ at 60 °C. As temperature increased, the ion movements became faster, leading to an increase in conductivity. Furthermore, it can be observed that the conductivity first surge and then slow down as the temperature increases. When the temperature rising from $-10$ °C to 10 °C, the frozen water gradually transformed to free water, which had a great influence on ion migration and led to a surge in conductivity. In the range above 10 °C, since the electrolytes were all in nonfrozen state, the conductivity increased relatively slowly as temperature increased.[45,46]

In comparison with conventional hydrogels, the temperature tolerance of PAAm-Clay-T

hydrogel, including anti-freezing and non-drying capability, was enhanced by the strong hydrogen bond interactions from the introduction of trehalose into the hydrogel networks. The PAAm-Clay-T hydrogel freezes at about −35 °C which is well below the freezing point of water, demonstrating the anti-freezing capability (Figure S4, Supporting Information). In addition, even though the PAAm-Clay-T hydrogel was stored at 60 °C for several hours, it could still maintain flexibility without being dried out. The trehalose could effectively hinder the formation of ice lattice and slow down the evaporation of water from hydrogels.[33] Therefore, the migration of ions could be well preserved across a broad temperature range, leading to good conductivity.

The conductivity restoration of the PAAm-Clay-T hydrogel during the process of cut and contact was investigated. As shown in Figure 2i, the PAAm-Clay-T hydrogel can serve as a conductor to connect the green light-emitting diode (LED) bulb and power source. Upon the hydrogel breakage, the LED turned off. Once the hydrogel was brought together, the LED lightened on again. The resistance change could further demonstrate the recovery of conductivity. After the hydrogel was cut, the resistance became infinite, owing to the open circuit. When the two halves were put into full contact, the conductivity rapidly restored within 0.2 s. Moreover, after undergoing the repeat process of cut and self-heal, the resistance of PAAm-Clay-T hydrogel could be maintained (Figure 2j and 2k). It can be concluded that due to the dynamic characteristic of hydrogen bonds, the electrical property of the hydrogel could well recover to the initial states. Overall, the PAAm-Clay-T hydrogel exhibited excellent self-healing ability in terms of both mechanical and electrical properties.

Adhesiveness is in favor of hydrogel to construct wearable devices to apply in human-machine interfaces and soft robots. The self-adhesive property of PAAm-Clay-T hydrogel on various substrates was investigated. As shown in **Figure 3**a, the PAAm-Clay-T hydrogel can tightly adhere to the surface of Al, IH-PUa, Latex, polydimethylsiloxane (PDMS), and Kapton. The adhesion strength was quantitatively measured by the lap shear test with the hydrogel

sandwiched between the substrates (Figure 3b). Figure 3c presents the adhesion force–displacement curves of PAAm-Clay-T hydrogel on various substrates. Then the adhesion strength can be calculated, and the values are 16.6 kPa on Al, 17.9 kPa on IH-PUa, 16.8 kPa on Latex, 16.4 kPa on PDMS, and 17.2 kPa on Kapton, respectively (Figure 3d). The strong adhesion between the hydrogel and substrates could be attributed to the interfacial physical interactions. The PAAm-Clay-T hydrogel had abundant polar groups including -OH, -NH$_2$, and -C=O, which could form metal coordination, hydrogen bonds, or dipole–dipole interactions with different substrates, thus achieving good interfacial bonding.[47,48] Benefiting from the excellent self-adhesiveness, it is convenient for the PAAm-Clay-T hydrogel to integrate with polymer or metal materials for the assembly of electronic devices without additional treatment processes.

## 2.4. Multimodal sensing

Both the IH-PUa polymer and conductive PAAm-Clay-T hydrogel are flexible, stretchable, and self-healing, making fully self-healing and conformable sensors a great possibility. Due to the strain and temperature responsiveness of conductive hydrogels, as well as the triboelectric property of polymers, multimodal sensors toward robotics for perception and motion monitoring could be achieved. The multimodal sensor can be constructed by IH-PUa polymer and PAAm-Clay-T hydrogel, which are served as encapsulation and electrode layers, respectively (**Figure 4**a). The PAAm-Clay-T electrode performed a sensing function. The encapsulation could protect the inner electrode and play a part in triboelectricity. Figure 4 presents the electrical response of the piezoresistive effect-based sensor with an area of 10 mm × 25 mm upon mechanical deformation. As shown in Figure 4b, the relative resistance change ($\Delta R/R_0$) almost increases linearly within the stretching strain from 0 to 200%. Due to the ionic transportation mechanism, the resistance of the sensor changed upon stretching. When the sensor was stretched, the ion transport channels in the cross-linked hydrogel networks changed,

leading to a decrease in ion concentration and thus an increase in resistance.[49] The gauge factor (GF) can be calculated according to the slope of the $\Delta R/R_0$ versus strain, which can be used to evaluate the sensing sensitivity for piezoresistive strain sensors.[35] The GF of the sensor was about 1.86 when the strain was in the range of 0 to 200%, indicating good sensing sensitivity. Owing to the temperature-tolerant properties of the PAAm-Clay-T hydrogel, the sensor could maintain the strain responsiveness after being stored at −10 °C for 2 h or 60 °C for 2 h. In addition, the GF of the self-healed sensor did not fluctuate much. These results further demonstrated that no matter whether the sensor went through temperature changes or the healing process, the electrical performance of the sensor could be maintained.

Figure 4c depicts the relative resistance change during the stretching−releasing cycles under a constant stretching strain of 50% with a tensile rate of 20 mm min$^{-1}$, 30 mm min$^{-1}$, and 60 mm min$^{-1}$, respectively. Regardless of the low or high tensile rate, the sensor could generate reproducible signals with a maximum relative resistance change of about 85%, verifying that the stretching rate had little influence on the relative resistance change. In addition, under both slight strain (1%, 3%, and 5%) and large strain (10%, 50%, 100%, and 150%), the relative resistance change was repeatable and stable, as shown in Figure 4d. In addition to stretching, the sensor could be bent with the electrical signals changing. As the flexion angle increases to 90 °, the relative resistance change reaches 40% (Figure 4e). The above results indicated that the PAAm-Clay-T hydrogel and IH-PUa could well function as the flexible electrode and encapsulation layer of the sensor, respectively, associated with good temperature tolerance and self-healing ability.

The as-fabricated sensor could be conformally equipped to the human body and accommodate to posture changes to detect human motions. As shown in Figure 4f, when the sensor is attached to the proximal interphalangeal joint of the index finger, with the finger bending angle increasing from 0 ° to 20 °, 30 °, 45 °, 60 °, and 90 °, the relative resistance change gradually increases and finally reaches 38%, exhibiting good responsiveness to angles. In

addition, the sensor could monitor the hand motion of stretching and clenching. The sensor was attached to the metacarpophalangeal joint. As shown in Figure 4g, when the hand state changes from stretching to clenching, the relative resistance change rapidly increases from 0 to 30%, and shows excellent repeatability and stability during the hand motion cycles. Moreover, the sensor could be used to transmit information from Morse code which is composed of specific combinations of dots and dashes to represent the corresponding alphabet. When the finger was bent and then quickly straightened, a clear spike signal of relative resistance change could be observed, which represented the dots of Morse code. When the finger was bent and held for seconds, a platform appeared with the resistance remaining constant, which represented the dashes of Morse code. The message "SMILE" could be acquired from the relative resistance change of the sensor when the finger is rhythmically bent (Figure 4h).

In addition to the human hand, the sensor could also be attached to the robotic hand to perceive temperature and gesture. The sensor adhered to the inner sides of the middle finger of the robotic hand which could hold a cup of ice water or hot water. In the thermoresistive mode, when the sensor touches the ice water (below −9.7 °C), the temperature of the sensor decreases to about 10 °C and the resistance rises (**Figure 5**a and 5c). When the sensor touches the hot water (up to 66.2 °C), the temperature of the sensor increases to about 45.8 °C and the resistance reduces (Figure 5b and 5c). Once the robotic hand releases the water, the resistance of the sensor could gradually restore, indicating the temperature sensing ability. The temperature responsiveness of the sensor originated from the thermoresistive effect, where the temperature could influence ion mobility rate, leading to the resistance of the sensor changing. The ion mobility rate increased with rising temperature, resulting in the decrease in the resistance of the hydrogel.[50] Furthermore, the sensor could be used to monitor the different gestures. As shown in Figure 5d, five sensors were attached to the joint of the robotic hand including the thumb, index, middle, ring, and little finger, respectively. When the robotic hand conducted the number of gestures changing from 1, 2, 3, 4, to 5, the relative resistance change of each sensor was

recorded. Through synthetically analyzing the electrical signals ($\Delta R/R_0$) caused by the finger flexion, the gesture could be identified.

Based on the coupling effect of contact electrification and electrostatic induction, the sensor could work in triboelectric mode to achieve self-powered sensing,[18] the mechanism of which is schematically illustrated in **Figure 6**a. The triboelectric sensor performed in single-electrode mode which could convert mechanical stimulus into electrical signals, and the IH-PUa and PAAm-Clay-T functioned as the electrification and electrode layer, respectively. When the sensor fully contacts with other material, equal positive and negative charges generate at the two surfaces, respectively, owing to different electron affinities (Figure 6a-i). Upon the contact material separating from the sensor, the ions in the hydrogel are induced to move to balance the static charges on the insulating IH-PUa. Meanwhile, the electrical double layer (EDL) could form at the interface of hydrogel and metal wire, with electrons flowing from ground to metal wire (Figure 6a-ii). Subsequently, the electrostatic balance can be reached when the two electrification layers completing separation (Figure 6a-iii). When the contact material is approaching back to the sensor, electrons flow in opposite directions (Figure 6a-iv). During repeat contact and separation process between PDMS and the sensor with the area of 40 mm × 40 mm under the frequency of 3 Hz, the alternating electrical signals generated, with the open-circuit voltage ($V_{oc}$) of 86 V (Figure 6b), short-circuit current ($I_{sc}$) of 6.7 μA (Figure 6c), and short-circuit charge ($Q_{sc}$) of 42 nC (Figure 6d). With the external resistance increasing from 39 kΩ to 10 GΩ, the output voltage rises and current decreases (Figure 6e). The maximum value of the power density reaches 171 mW m$^{-2}$ at 30 MΩ (Figure 6f). Due to the self-healing properties of the electrification and electrode layers, the sensor that was cut in half and then brought together for repair showed almost the same voltage peak value as the original sample. In addition, the sensor could maintain the output electrical performances after being stored at −10 ºC for 2 h or 60 ºC for 2 h, which could be ascribed to the temperature-tolerant properties of the PAAm-Clay-T hydrogel (Figure 6g). Owing to the electron affinity difference between

materials, when the self-powered sensor interacted with different materials such as PDMS, polyethylene terephthalate (PET), polymethyl methacrylate (PMMA), Kapton, glass, paper, and Al, a differentiated electrical signal could be generated (Figure 6h). The sensor exhibited excellent electrical performances whether operating in piezoresistive or triboelectric mode.

It is worth noting that the sensor could be integrated with the soft robot to detect its motions and different materials. A pneumatically actuated quadrupedal soft robot[51] was fabricated, which was based on the pneu-net (PN) architecture and contained five pneumatic channels. As shown in **Figure 7**a and 7b, five sensor units, each consisting of a layer of IH-PUa and a layer of PAAm-Clay-T hydrogel, are adhered to the PDMS surface of the soft robot. The design model and the preparation process of the soft robot were described in Supporting Information. The sensors can well adapt to dynamically curved surfaces, showing outstanding conformable properties (Figure 7c and 7d). Air was regularly pumped into the five pneumatic channels to control the soft robot to crawl, with its four legs (PN1, PN2, PN4, and PN5) and main body (PN3) repeatedly bending and straightening. During the soft robot crawling, seven typical moments were captured and the electrical signals were recorded. As shown in Figure 7e, the relative resistance change collected from the five sensors can reflect the various poses of the soft robot.

In addition to the piezoresistive mode, the sensor integrated on the soft robot could operate in triboelectric mode, enabling self-powered sensing to perceive different materials. The schematic illustration of the working mechanism is depicted in Figure 7f. When the sensor contacting or separating from the material, a potential difference could be built and the electrons flowed at the external circuit, resulting in detectable electrical signals. Therefore, during the contact and separation process of the sensor with various materials, electrical signals with different peak values could be detected. In this context, the sensor on the main body of the soft robot was tracked when contacting different materials. During the soft robot crawling, inflation and deflation were conducted, leading to the contact and separation between the sensor and the

material. As shown in Figure 7g, different voltage signals can be observed when the sensor touches different materials including PDMS, PET, PMMA, Kapton, glass, paper, and Al, indicating the ability of the sensor to be integrated with soft robots to sense materials. Overall, the sensor could operate in piezoresistive, thermoresistive, or triboelectric mode to detect different signals, such as strain, temperature, and materials. Compared with the previously reported self-healing and stretchable sensors, most of which were not entirely self-healing, not multifunctional, or not adapted for soft robots, the as-fabricated multimodal sensor shows outstanding comprehensive performances (the detail comparison in Table S1, Supporting Information). These results demonstrated that the multimodal sensor with flexible, self-healing, temperature-resisted, stretchable, and conformable properties shows broad prospects in wearable devices, human-machine interfacing, and robotics.

## 3. Conclusion

In summary, an entirely intrinsic self-healing, stretchable, attachable, and conformable multimodal sensor with deformation, temperature, motions, and materials sensing ability for robotics was developed. The sensor was composed of the dynamic bonds-based IH-PUa polymer and PAAm-Clay-T hydrogel. The reversibility of the dynamic bonds (imine and hydrogen bonds) led to the self-healing ability of the materials with the self-healing efficiency above 98%. Both IH-PUa and PAAm-Clay-T showed high stretchability with the fracture strain up to 1028% and 4052%, respectively. The PAAm-Clay-T hydrogel as the electrode could transfer charges with the high conductivity of $9.95 \times 10^{-2}$ S cm$^{-1}$ at 25 $^{\circ}$C, and sense deformation with the GF value of 1.86. Even if the sensor suffered mechanical damage or high or low temperature, the sensing capability of the sensor could be restored whether operating in piezoresistive or triboelectric mode, due to the self-healing ability and temperature tolerance. Based on the dependence of ion migration on temperature, the sensor could sense hot and cold conditions. Owing to the adhesiveness of the PAAm-Clay-T hydrogel, strong interfacial

15

bonding could be formed between IH-PUa and PAAm-Clay-T with the adhesion strength up to 17.9 kPa and the sensor could be conveniently assembled. Meanwhile, the PAAm-Clay-T hydrogel showed good adhesion on various materials, enabling the sensor to be well attached to the robots. The sensor possessed good conformability and could adapt to dynamically curved surfaces, which guaranteed that the sensor could work effectively during the robot motion. Various postures including hand bending and soft robot crawling, the information of Morse code, the temperature of objects, and the type of materials could be identified by the electrical signals collected from the sensors. This work opens up new avenues for the construction of reliable and flexible multimodal sensors by functional polymers for robotics.

**Supporting Information**

Supporting Information is available from the Wiley Online Library or from the author.

**Acknowledgments**

**Conflict of Interest**

The authors declare no conflict of interest.

**Data Availability Statement**

The data supporting the findings of this study are available within the paper and also available from the corresponding authors upon reasonable request.

**References**

[1]    A. G. C. Gonzalez, M. V. S. Alves, G. S. Viana, L. K. Carvalho, J. C. Basilio, *IEEE T. Ind. Inform.* **2018**, *14*, 1732.

[2]    A. Kotikian, C. McMahan, E. C. Davidson, J. M. Muhammad, R. D. Weeks, C. Daraio, J. A. Lewis, *Sci. Robot.* **2019**, *4*, eaax7044.

[3]    C. M. Boutry, M. Negre, M. Jorda, O. Vardoulis, A. Chortos, O. Khatib, Z. N. Bao, *Sci. Robot.* **2018**, *3*, eaau6914

[4]    H. Bai, Y. S. Kim, R. F. Shepherd, *Sci. Adv.* **2022**, *8*, eabq2104.

[5]    Y. Dong, L. Wang, N. Xia, Z. Yang, C. Zhang, C. Pan, D. Jin, J. Zhang, C. Majidi, L. Zhang, *Sci. Adv.* **2022**, *8*, eabn8932.

[6]    Q. Shi, B. Dong, T. He, Z. Sun, J. Zhu, Z. Zhang, C. Lee, *InfoMat* **2020**, *2*, 1131.

[7]    T. Jin, Z. Sun, L. Li, Q. Zhang, M. Zhu, Z. Zhang, G. Yuan, T. Chen, Y. Tian, X. Hou, C. Lee, *Nat. Commun.* **2020**, *11*, 5381.

[8]    X. Qu, J. Xue, Y. Liu, W. Rao, Z. Liu, Z. Li, *Nano Energy* **2022**, *98*, 107324.

[9]    W. Gao, H. Ota, D. Kiriya, K. Takei, A. Javey, *Acc. Chem. Res.* **2019**, *52*, 523.

[10]  X. Dai, L.-B. Huang, Y. Du, J. Han, J. Kong, *Compos. Commun.* **2021**, *24*, 100654.

[11]  J. Zhang, L. Wan, Y. Gao, X. Fang, T. Lu, L. Pan, F. Xuan, *Adv. Electron. Mater.* **2019**, *5*, 1900285.

[12]  C. Wang, C. Pan, Z. Wang, *ACS Nano* **2019**, *13*, 12287.

[13] X. Dai, L.-B. Huang, Z. Sun, Y. Du, B. Xue, M. C. Wong, J. Han, Q. Liang, Y. Wu, B. Dong, J. Kong, J. Hao, *Mater. Horiz.* **2022**, *9*, 2603.

[14] Y. Z. Cao, T. Z. Bu, C. L. Fang, C. Zhang, X. D. Huang, C. Zhang, *Adv. Funct. Mater.* **2020**, *30*, 2002613.

[15] Q. Su, Q. Zou, Y. Li, Y. Chen, S. Y. Teng, J. T. Kelleher, R. Nith, P. Cheng, N. Li, W. Liu, S. Dai, Y. Liu, A. Mazursky, J. Xu, L. Jin, P. Lopes, S. Wang, *Sci. Adv.* **2021**, *7*, eabi4563.

[16] Y. Wu, X. Dai, Z. Sun, S. Zhu, L. Xiong, Q. Liang, M.-C. Wong, L.-B. Huang, Q. Qin, J. Hao, *Nano Energy* **2022**, *98*, 107240.

[17] J. C. Yang, J. Mun, S. Y. Kwon, S. Park, Z. Bao, S. Park, *Adv. Mater.* **2019**, *31*, 1904765.

[18] X. Wei, B. Wang, Z. Wu, Z. L. Wang, *Adv. Mater.* **2022**, *34*, 2203073.

[19] Z. Liu, Y. Wang, Y. Ren, G. Jin, C. Zhang, W. Chen, F. Yan, *Mater. Horiz.* **2020**, *7*, 919.

[20] Z. X. Wu, H. Wang, Q. L. Ding, K. Tao, W. X. Shi, C. Liu, J. Chen, J. Wu, *Adv. Funct. Mater.* **2023**, *33*, 2300046.

[21] Z. Yu, P. Wu, *Adv. Mater.* **2021**, *33*, 2008479.

[22] L.-B. Huang, X. Dai, Z. Sun, M.-C. Wong, S.-Y. Pang, J. Han, Q. Zheng, C.-H. Zhao, J. Kong, J. Hao, *Nano Energy* **2021**, *82*, 105724.

[23] J. Zhao, T. Bu, X. Zhang, Y. Pang, W. Li, Z. Zhang, G. Liu, Z. L. Wang, C. Zhang, *Research* **2020**, *2020*, 1398903.

[24] H. Chen, P. Ge, Z. Yan, M. Chen, X. Dai, H. Zhuo, S. Chen, L.-B. Huang, T. Zhang, *Chem. Eng. J.* **2022**, *430*, 133111.

[25] P. Zhang, I. M. Lei, G. Chen, J. Lin, X. Chen, J. Zhang, C. Cai, X. Liang, J. Liu, *Nat. Commun.* **2022**, *13*, 4775.

[26] J. Deng, H. Yuk, J. Wu, C. E. Varela, X. Chen, E. T. Roche, C. F. Guo, X. Zhao, *Nat. Mater.* **2021**, *20*, 229.

[27] H. Yuk, J. Wu, X. Zhao, *Nat. Rev. Mater.* **2022**, *7*, 935.

[28] C. Xie, X. Wang, H. He, Y. Ding, X. Lu, *Adv. Funct. Mater.* **2020**, *30*, 1909954.

[29] T. Zhu, Y. Ni, G. M. Biesold, Y. Cheng, M. Ge, H. Li, J. Huang, Z. Lin, Y. Lai, *Chem. Soc. Rev.* **2023**, *52*, 473.

[30] Q. Peng, J. Chen, T. Wang, X. Peng, J. Liu, X. Wang, J. Wang, H. Zeng, *InfoMat* **2020**, *2*, 843.

[31] K. Tao, Z. Chen, J. Yu, H. Zeng, J. Wu, Z. Wu, Q. Jia, P. Li, Y. Fu, H. Chang, W. Yuan, *Adv. Sci.* **2022**, *9*, 2104168.

[32] F. Chen, D. Zhou, J. Wang, T. Li, X. Zhou, T. Gan, S. Handschuh-Wang, X. Zhou, *Angew. Chem. Int. Edit.* **2018**, *57*, 6568.

[33] Z. Han, P. Wang, Y. Lu, Z. Jia, S. Qu, W. Yang, *Sci Adv* **2022**, *8*, eabl5066.

[34] Z. Shen, Z. Zhang, N. Zhang, J. Li, P. Zhou, F. Hu, Y. Rong, B. Lu, G. Gu, *Adv. Mater.* **2022**, *34*, 2203650.

[35] K. Zhai, H. Wang, Q. Ding, Z. Wu, M. Ding, K. Tao, B. R. Yang, X. Xie, C. Li, J. Wu, *Adv. Sci.* **2022**, *10*, 2205632.

[36] Q. Zheng, X. Dai, Y. Wu, Q. Liang, Y. Wu, J. Yang, B. Dong, G. Gao, Q. Qin, L.-B. Huang, *BMEMat* **2023**, *1*, e12008.

[37] W. Xu, M.-C. Wong, J. Hao, *Nano Energy* **2019**, *55*, 203.

[38] X. Dai, L.-B. Huang, Y. Du, J. Han, Q. Zheng, J. Kong, J. Hao, *Adv. Funct. Mater.* **2020**, *30*, 1910723.

[39] X. Dai, Y. Du, Y. Wang, Y. Liu, N. Xu, Y. Li, D. Shan, B. B. Xu, J. Kong, *ACS Appl. Polym. Mater.* **2020**, *2*, 1065.

[40] J. Zhao, J. Zeng, L. Chen, Y. Lin, Z. B. Zhang, C. Zhang, *Mater. Today Phys.* **2022**, *28*, 100877.

[41] R. Du, Z. Xu, C. Zhu, Y. Jiang, H. Yan, H. C. Wu, O. Vardoulis, Y. Cai, X. Zhu, Z. Bao, Q. Zhang, X. Jia, *Adv. Funct. Mater.* **2020**, *30*, 1907139.

[42] X. Dai, Y. Du, J. Yang, D. Wang, J. Gu, Y. Li, S. Wang, B. B. Xu, J. Kong, *Compos. Sci. Technol.* **2019**, *174*, 27.

[43] J. Kang, D. Son, G. N. Wang, Y. Liu, J. Lopez, Y. Kim, J. Y. Oh, T. Katsumata, J. Mun, Y. Lee, L. Jin, J. B. Tok, Z. Bao, *Adv. Mater.* **2018**, *30*, 1706846.

[44] X. Sui, H. Guo, P. Chen, Y. Zhu, C. Wen, Y. Gao, J. Yang, X. Zhang, L. Zhang, *Adv. Funct. Mater.* **2019**, *30*, 1907986.

[45] J. B. Yang, Z. Xu, J. J. Wang, L. G. Gai, X. X. Ji, H. H. Jiang, L. B. Liu, *Adv. Funct. Mater.* **2021**, *31*.

[46] Y. Jian, S. Handschuh-Wang, J. Zhang, W. Lu, X. Zhou, T. Chen, *Mater. Horiz.* **2021**, *8*, 351.

[47] S. Xia, S. Song, F. Jia, G. Gao, *J. Mater. Chem. B* **2019**, *7*, 4638.

[48] L. M. Zhang, Y. He, S. Cheng, H. Sheng, K. Dai, W. J. Zheng, M. X. Wang, Z. S. Chen, Y. M. Chen, Z. Suo, *Small* **2019**, *15*, 1804651.

[49] Y. Ou, T. Zhao, Y. Zhang, G. Zhao, L. Dong, *Mater. Horiz.* **2022**, *9*, 1679.

[50] X. Ma, C. Wang, R. Wei, J. He, J. Li, X. Liu, F. Huang, S. Ge, J. Tao, Z. Yuan, P. Chen, D. Peng, C. Pan, *ACS Nano* **2022**, *16*, 2789.

[51] R. F. Shepherd, F. Ilievski, W. Choi, S. A. Morin, A. A. Stokes, A. D. Mazzeo, X. Chen, M. Wang, G. M. Whitesides, *Proc. Natl. Acad. Sci. U.S.A.* **2011**, *108*, 20400.
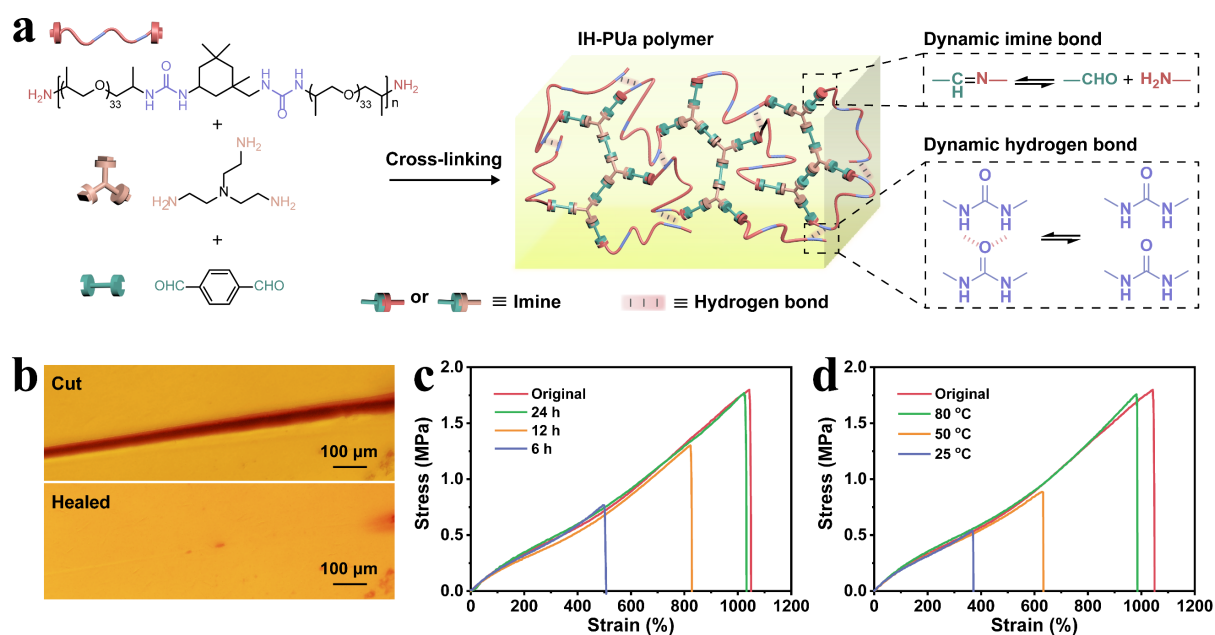
**Figure 1.** Design and performance of IH-PUa polymer. a) Schematic illustration of the cross-linked IH-PUa polymer networks based on dynamic imine and hydrogen bonds. b) Optical microscopic images before and after self-healing. c) Tensile testing results of the original and broken specimens after undergoing different healing times at 25 $^{\circ}$C. d) Tensile testing results of the original and broken specimens after healing for 3 h at different temperatures.
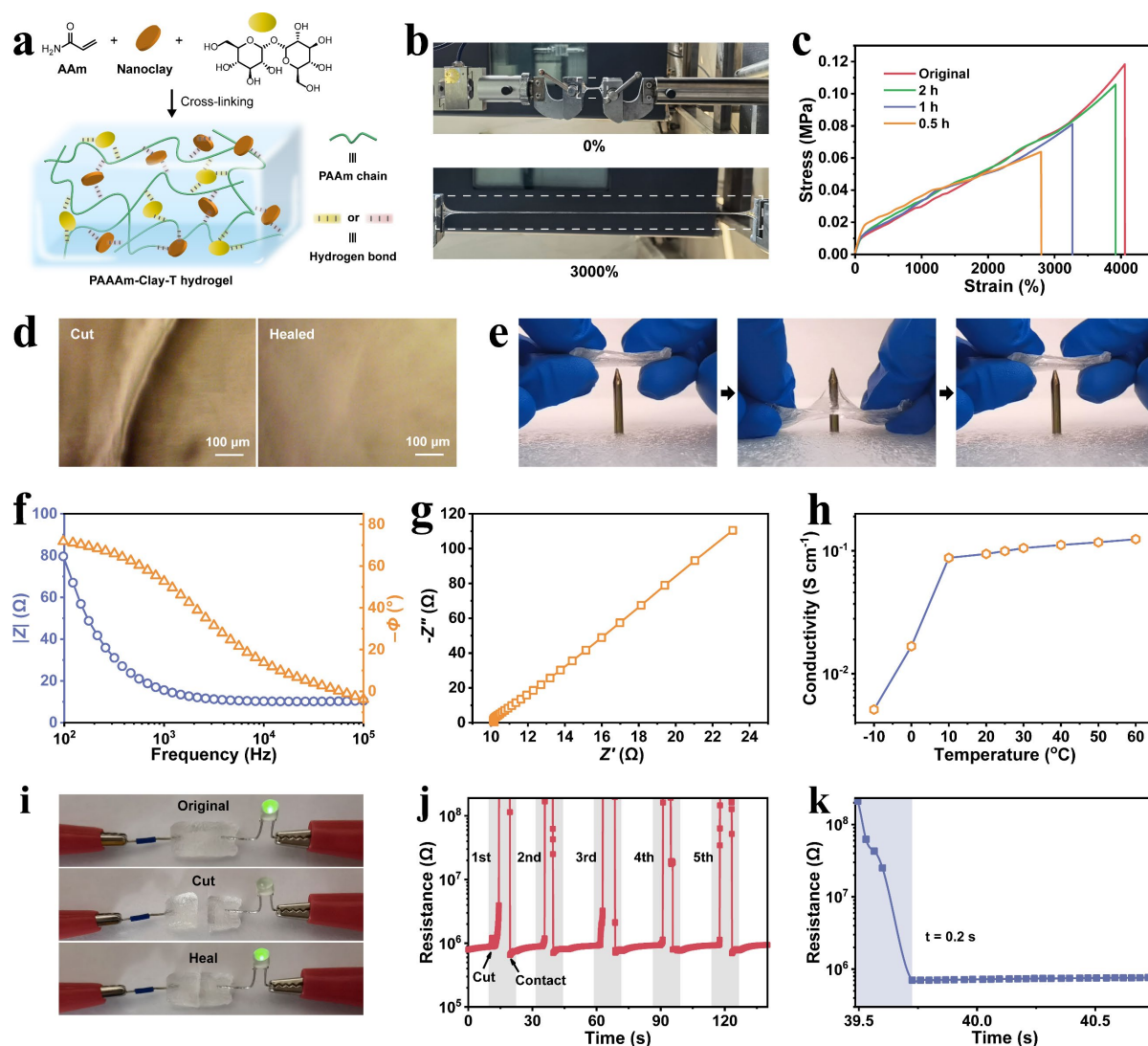
**Figure 2.** Design and performance of PAAm-Clay-T hydrogel. a) Schematic illustration of hydrogen bond-based PAAm-Clay-T hydrogel formed by the polymerization of AAm, nanoclay, and trehalose. b) Optical images when stretching from 0 to 3000%. c) Tensile testing results of the original and broken specimens after undergoing different healing times. d) Optical microscopic images before and after self-healing. e) Images showing the puncture-resistance. f) Plots of impedance magnitude ($|Z|$, purple line) and negative phase angle ($-\phi$, orange line) versus testing frequency. g) Nyquist plot of impedance spectrum at room temperature. h) Plots of conductivity versus testing temperature from $-10\ ^{\circ}C$ to $60\ ^{\circ}C$. i) PAAm-Clay-T hydrogel as a conductor in series with a green LED bulb under a voltage of 2 V when in original, cut, healed states. j) Resistance change upon repeated cutting and contacting. k) Electrical healing time.
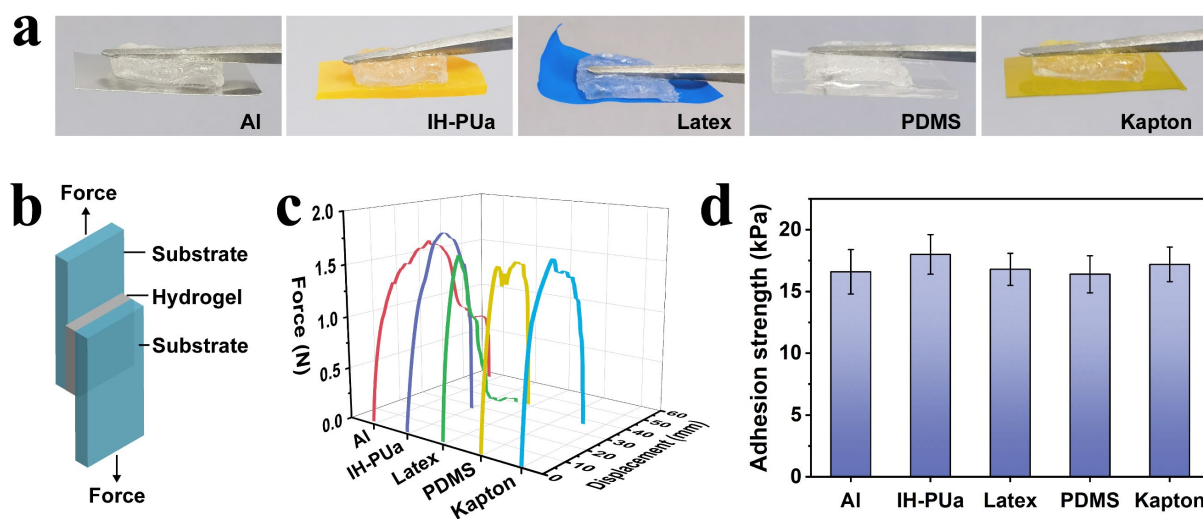
**Figure 3.** Adhesive performance. a) Photographs of PAAm-Clay-T hydrogel adhered on the surface of Al, IH-PUa, Latex, PDMS, and Kapton. b) Schematic illustration of lap shear test. c) Adhesion force–displacement curves of PAAm-Clay-T hydrogel on various substrates. d) Adhesion strength of PAAm-Clay-T hydrogel on various substrates.
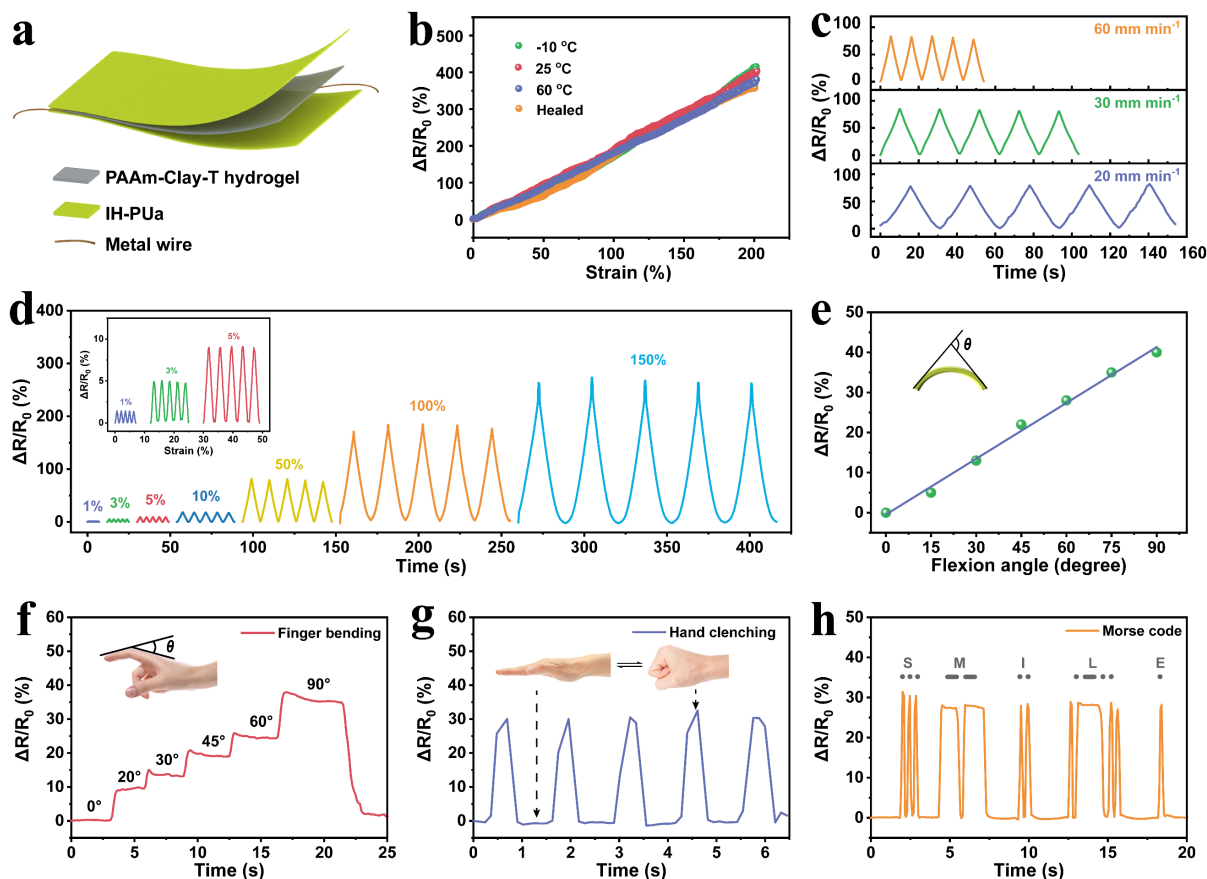
**Figure 4.** Sensing performance based on piezoresistive effect and demonstration of the sensor for monitoring human motion. a) Schematic diagram of the sandwich-structured sensor. b) Relative resistance change versus tensile strain of the sensor after being stored at different temperatures (−10 °C, 25 °C, and 60 °C) and undergoing a self-healing process. c) Relative resistance change under different stretching rates (20 mm min$^{-1}$, 30 mm min$^{-1}$, and 60 mm min$^{-1}$). d) Relative resistance change under various strains (1%, 3%, 5%, 10%, 50%, 100%, and 150%). e) Relative resistance change versus flexion angle. f) Relative resistance change during the finger bending angle ranging from 0° to 90°. g) Relative resistance change when hand clenching. h) Relative resistance change during the finger bending according to Morse code.
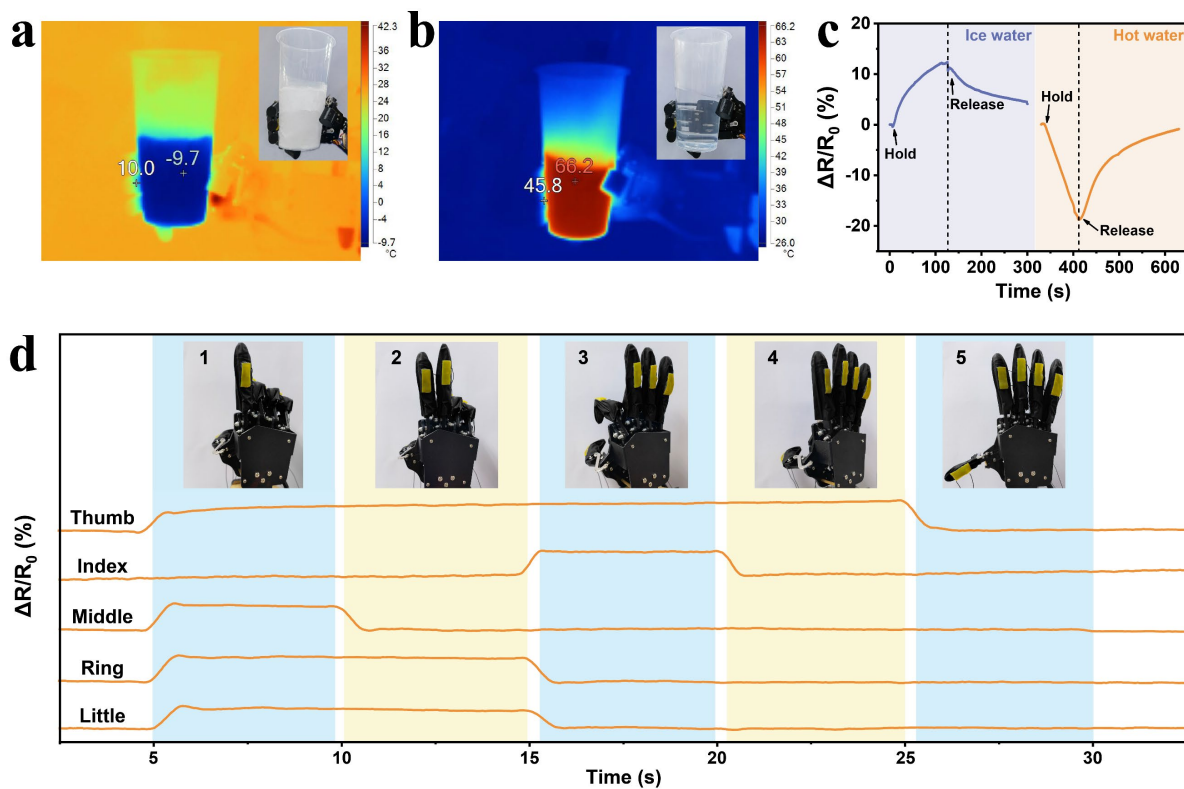
**Figure 5.** Demonstration of the sensor attached to the robotic hand for temperature and gesture recognition. Thermal images of the robotic hand attached to the sensor holding a cup of a) ice water and b) hot water. c) Relative resistance change during touching ice and hot water. d) Relative resistance change of the five sensors when the robotic hand in different gestures.
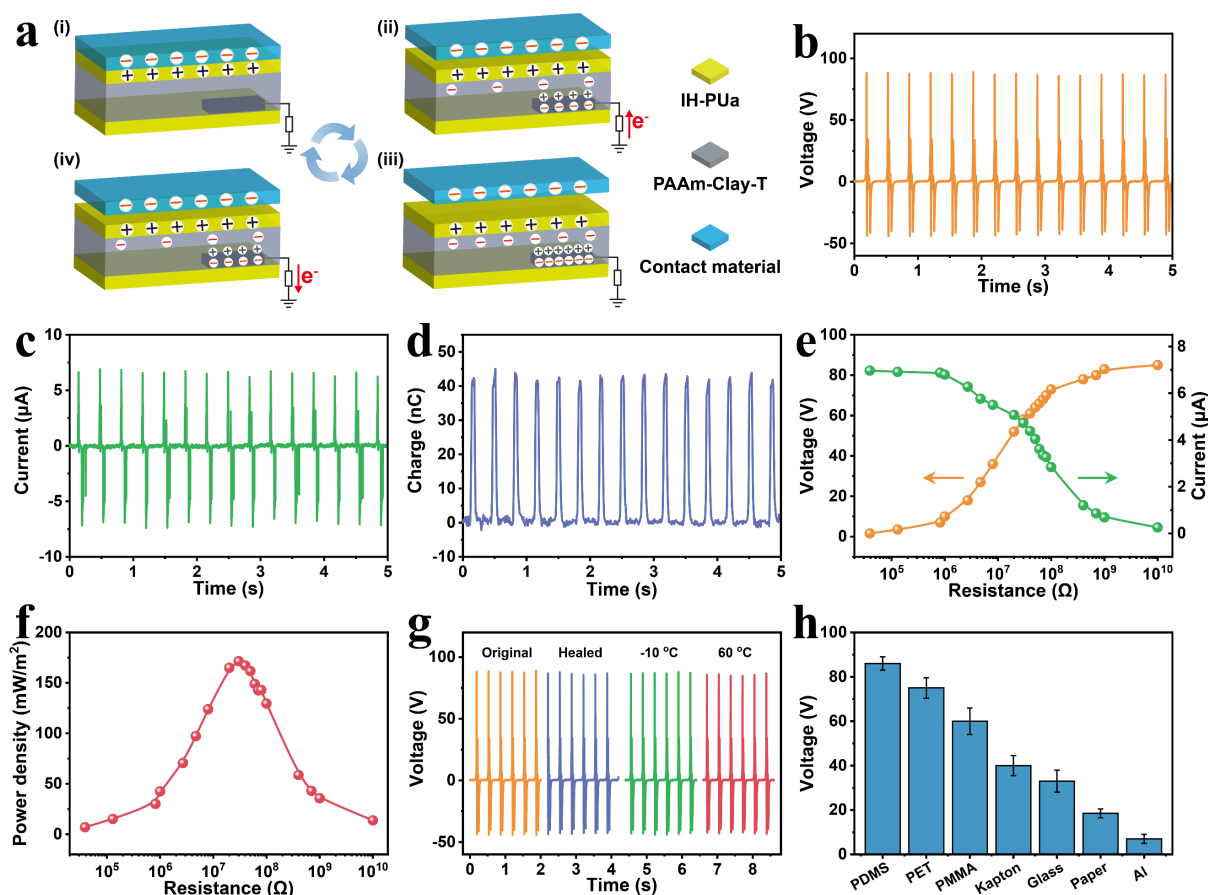
**Figure 6.** Sensor performances based on triboelectric effect. a) Working mechanisim of the triboelectric sensor. b) Open-circuit voltage, c) short-circuit current, and d) short-circuit transferred charge of the sensor under contact and separation with a frequency of 3 Hz. e) Varation of voltage and current with external resistance load. f) Power density with the resistance increaseing from 39 kΩ to 10 GΩ. g) Open-circuit voltage of the sensor after being stored at different temperatures (−10 °C and 60 °C) and undergoing a self-healing process. h) Open-circuit voltage of the sensor when contacting different materials.
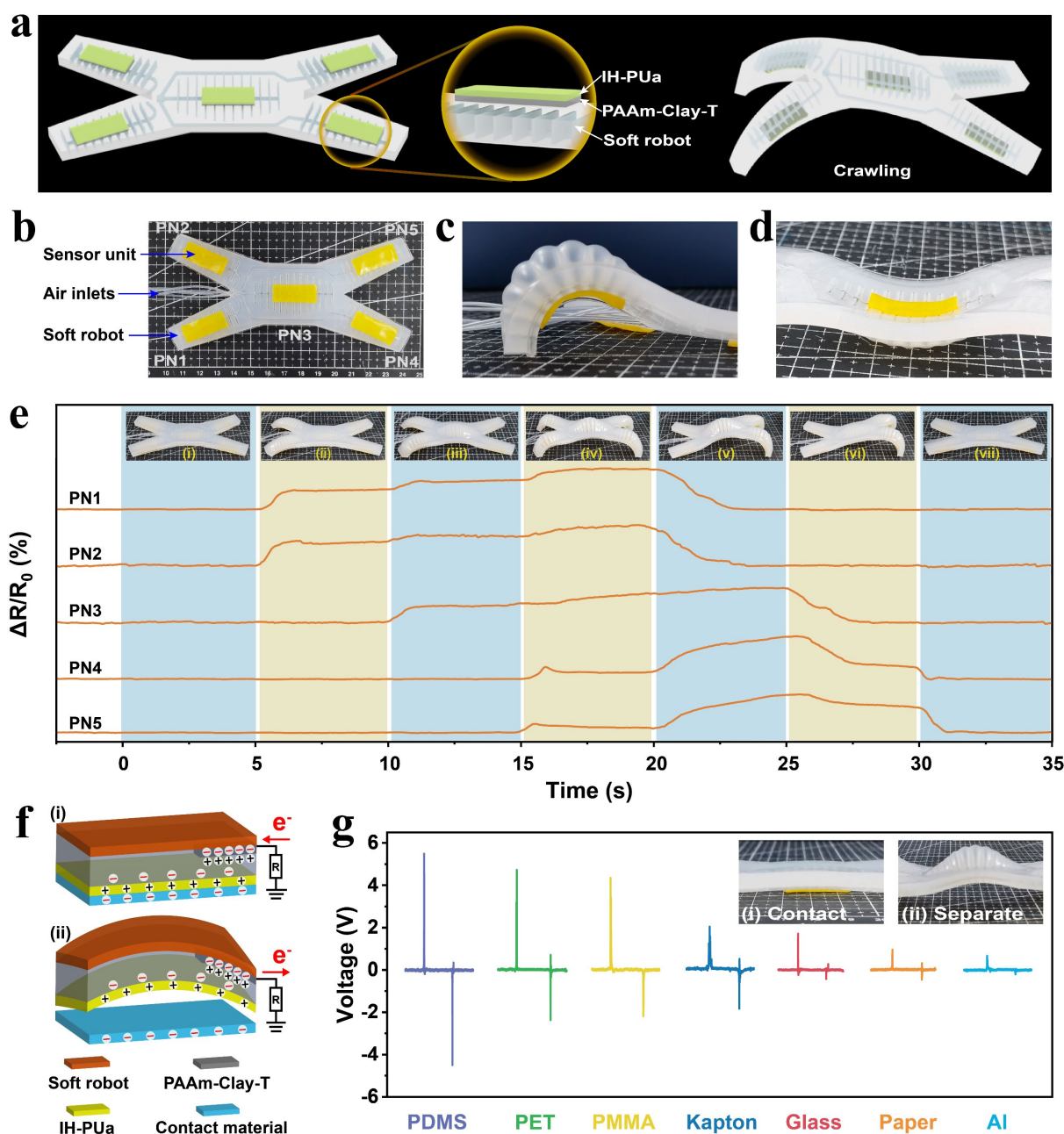
**Figure 7.** Demonstration of the sensors integrated with the soft robot for motion and material recognition. a) Schematic illustration of the sensors on the soft robot. b) Photographs of the five sensor units adhered on the surface of a pneumatically actuated quadrupedal soft robot. c) and d) Conformability of the sensor when soft robot curling. e) Relative resistance change of the five sensors during the soft robot crawling. f) Schematic illustration of the working mechanism of the sensor in triboelectric mode. g) Voltage outputs of the sensor when contacting various materials.